

# UNSTEADY TURBULENT SKIN FRICTION AND SEPARATION LOCATION MEASUREMENTS ON A MANEUVERING UNDERSEA VEHICLE

Serhat Hosder\* and Roger L. Simpson†

Department of Aerospace and Ocean Engineering  
Virginia Polytechnic Institute and State University  
Blacksburg, VA 24061

## Abstract

Steady and unsteady flow over a generic Suboff model is studied. The skin friction magnitudes are measured by using hot-film sensors each connected to a constant temperature anemometer. The local minima in the skin friction magnitudes are used to obtain the separation locations. Steady results are presented for two model configurations: barebody and sail-on-side case. Unsteady results are given for the barebody case. The dynamic plunge-pitch-roll model mount (DyPPiR) is used to simulate the pitchup maneuvers. The pitchup maneuver is a linear ramp from  $1^\circ$  to  $27^\circ$  in 0.33 seconds. Steady results show that the flow structure on the leeward side of the barebody can be characterized by the crossflow separation. In the sail-on-side case, the separation pattern of the non-sail region follow the barebody separation trend closely. The flow on the sail side is strongly affected by the presence of the sail and the separation pattern is different from the crossflow separation. Unsteady results show significant time lags between unsteady and steady separation locations. These effects produce the difference in separation topology between the unsteady and steady flowfields. A first-order time lag model approximates the unsteady separation locations reasonably well and time lags are obtained by fitting the model equation with the experimental data.

## Nomenclature

$A$	= hot-film sensor calibration coefficient, equation (4)
$B$	= hot-film sensor calibration coefficient, equation (4)
$a$	= model radius of the constant diameter region
$C_f$	= skin friction coefficient
$E$	= time-averaged voltage value
$F$	= generalized steady and quasi-steady aerodynamic vector function
$G$	= generalized unsteady aerodynamic vector function
$H$	= shape factor
$\bar{h}$	= mean heat transfer film coefficient

\*Graduate student, Student Member AIAA

†Jack E. Cowling Professor, Fellow AIAA

Copyright ©2001 by the authors. Published by the American Institute of Aeronautics and Astronautics, Inc. with permission.

$L$	= model length
$Re_a$	= radius based Reynolds number, $U_\infty a/\nu$
$Re_L$	= length based Reynolds number, $U_\infty L/\nu$
$Re_\theta$	= momentum thickness based Reynolds number, $U_\infty \theta/\nu$
$t'$	= non-dimensional time, $tU_\infty/L$
$t_{ref}$	= reference time, $L/U_\infty$
$T_\infty$	= free-stream temperature
$T_w$	= hot-film sensor temperature
$U_e$	= boundary layer edge velocity
$U_\infty$	= free-stream velocity
$x$	= model longitudinal position from nose
$x_{cg}$	= location of center of rotation
$z$	= DyPPiR plunge ordinate
$\alpha$	= model center angle of attack and DyPPiR pitch angle
$\alpha_{eff}$	= effective angle of attack, $\alpha_{eff} = \alpha - \Delta\alpha_{eff}$
$\dot{\alpha}$	= dimensional pitch rate
$\Delta\alpha_{eff}$	= incremental effective angle of attack
$\beta$	= sideslip angle
$\delta$	= boundary layer thickness
$\delta^*$	= displacement thickness
$\nu$	= kinematic viscosity
$\tau_w$	= wall shear stress
$\tau'$	= first-order time lag in non-dimensional units
$\theta$	= momentum thickness
$\phi$	= circumferential location on the model surface
$\phi_{sep}$	= separation location
$\phi_{uns}$	= approximation to the unsteady separation location, equation (8)
$\phi_0$	= quasi-steady separation location, equation (8)

## I. Introduction

The study of truly unsteady, high-excursion and high-Reynolds Number separated flows over undersea vehicles, aircraft or missiles has become of great importance in the analysis and the improvement of the dynamic performance. Because of highly complex, three-dimensional, turbulent and separated nature, standard stability derivative techniques fail to capture the nonlinearities in these flows and Computational Fluid Dynamics (CFD) techniques need physical models that can resolve the complexities of such flowfields in order to get accurate and more reliable results. Suitable simulation of the time-dependent maneuvers in the wind tunnels is not only important for understanding the physics of complex flow phenomena, but also supplies the necessary information required for developing the realistic unsteady phys-

ical flow models. The DyPPiR (Dynamic plunge-pitch-roll) model mount, a computer controlled, three degrees of freedom robotic arm at the Stability Wind Tunnel of Virginia Tech, provides the unique capability of performing pre-programmed general, high-excursion, large scale, high-Reynolds Number unsteady maneuvers.<sup>1</sup>

Dynamic testing has been an important part of design and validation of various types of craft for decades. Typically these techniques are only *quasi-steady*, relying on very small amplitude sinusoidal oscillations that can describe small-excursion maneuvers reasonably well.<sup>2</sup> As discussed by Wetzel and Simpson,<sup>3</sup> there is a significant difference between quasi-steady and unsteady aerodynamics. In a quasi-steady approach, the aerodynamics of a maneuvering body are dependent only on the instantaneous state of the model ( $\alpha$  angle of attack,  $\beta$  sideslip angle, control surface deflections, etc.), whereas in fully general unsteady aerodynamics, explicit time dependency, or history effects are also included. Mathematically the distinction between quasi-steady and unsteady aerodynamics can be shown as follows: steady,  $\mathbf{F}(\alpha, \beta, \dots)$ ; quasi-steady,  $\mathbf{F}[\alpha(\mathbf{t}'), \beta(\mathbf{t}'), \dots]$ ; and fully unsteady  $\mathbf{G}[\mathbf{t}', \alpha(\mathbf{t}'), \dot{\alpha}(\mathbf{t}'), \beta(\mathbf{t}'), \dot{\beta}(\mathbf{t}'), \dots]$  where  $\mathbf{F}$  and  $\mathbf{G}$  can be a dominant flow feature such as separation location. Here  $t'$  is the non-dimensional time given by:<sup>4</sup>

$$t' = \frac{t}{t_{ref}} = \frac{tU_\infty}{L} \quad (1)$$

$t_{ref}$  represents the time for the flow to pass over a model:  $L/U_\infty$ . The history effects mainly cause time lags or leads between the unsteady and the corresponding instantaneous quasi-steady flowfields, which can be quantified by measuring flow separation locations or the aerodynamic loads on a body undergoing time-dependent maneuvers.

Among the previous studies, the unsteady crossflow separation location measurements on a maneuvering 6:1 prolate spheroid model by Wetzel<sup>2</sup> can be considered as the most similar work to the one presented here in terms of the experimental measurement technique, model and the unsteady high-excursion maneuvers performed. In his work, he has determined significant lags in the unsteady flow separation locations on the prolate spheroid undergoing pitch-up and turning maneuvers compared with the steady data. Wetzel and Simpson<sup>3</sup> also found that a first-order lag model fits the unsteady data. A review of some other relevant studies of three-dimensional, unsteady aerodynamic experiments on various bodies has been given in Wetzel and Simpson,<sup>3</sup> and Hosder.<sup>5</sup>

In the present work, unsteady turbulent flow separation on a maneuvering undersea vehicle is studied. Hot-film sensors were used to measure the surface skin friction magnitude values over the body surface. Local minima of the skin friction magnitude values are used to determine the separation locations.<sup>6</sup> Steady skin friction measurements were obtained for different model-center angle of attacks. Unsteady maneuvers include the ramp pitchup maneuvers simulated by the DyPPiR. Surface oil flow visualizations were also used in order to examine

the steady surface flow topology and the separation locations qualitatively. Both steady and unsteady tests were performed for two model configurations: The barebody (axi-symmetric case) and the body with the sail. In this paper, the steady results for both cases are presented while the unsteady results and discussion are given for the barebody case.

## II. Experimental Apparatus and Techniques

### II.A. Wind Tunnel and the DyPPiR

Virginia Tech Stability Wind Tunnel with  $1.8 \times 1.8$  m square test section has been used for the experiments. The tunnel is a closed-return, closed test section subsonic facility powered by 450-kW dc motor driving a 4.27 m long propeller. Tunnel, with a maximum-speed of 80 m/s, has a very low free-stream turbulence level of 0.03%.<sup>1</sup> To eliminate flow blockage effects, a slotted wall test section was used with 38% open area ratio.

The Dynamic Plunge, Pitch and Roll actuator (DyPPiR) is installed in the Virginia Tech Stability Wind Tunnel (figure 1). This computer controlled model mount DyPPiR has three degrees of freedom: plunge with a vertical range of 1.5 m from the tunnel centerline, pitch with a range of  $\pm 45^\circ$  and (with recently made improvements) roll with a range of  $\pm 360^\circ$ . The three hydraulic actuators give the DyPPiR power to force a maximum model load of 45 kg and 250 kg of hardware at rates approaching to 9 m/s in plunge and 120 degs/s in pitch. By the combined motion of pitch and plunge actuators, the DyPPiR can perform maneuvers around an arbitrary center of rotation, which is important for obtaining the correct lateral velocities across the aircraft and the submarines. These unique features of the DyPPiR allows one to simulate the pre-programmed, general, high-excursion, rapid, time-dependent maneuvers and to keep the model in desired location and orientation in steady testing as well. The coordinate nomenclature for the DyPPiR and the model is given in figure 2. Note that the circumferential location  $\phi$  is measured from the windward line of symmetry in the counter-clockwise direction.

### II.B. Wind Tunnel Model

The light weight model has a generic Suboff undersea vehicle geometry with a scaled length ( $L$ ) of 2.24 m. The model has a bow region for  $0.0 \leq (x/L) \leq 0.23$ , a constant diameter region for  $0.23 \leq (x/L) \leq 0.75$  and an afterbody (stern) region for  $0.75 \leq (x/L) \leq 1.0$ . The sail can be detached, resulting in the axis-symmetric configuration of the model which can be thought as a missile or to a certain extent an aircraft fuselage geometry (figure 4). Figure 3 shows the model geometry with the hot-film sensor locations. More sensors have been used near the body-sail junction region to resolve the complex structure of the separated flow. Oil flow visualization

pictures also have been used in order to determine the optimum sensor locations.

The barebody measurements have been performed by using 15 sensors located at certain positions on the long row (figure 3). The same sensors have been used in the sail-on-side case throughout the whole circumferential locations. The remaining sensors were used near the sail region in order to resolve the flow structure. For the sail-on-side configuration, the chordline of the sail is aligned with the circumferential location  $\phi = 270^\circ$ . At its maximum thickness location, the sail extends from  $\phi = 262^\circ$  to  $278^\circ$  and is placed between  $x/L = 0.21$  and  $x/L = 0.31$ .

The sail is mounted on a movable ring integrated into the model structure and can be rotated and fixed to any desired circumferential location. Both in steady and unsteady testing, the skin friction distribution on the whole surface of the model with desired circumferential spacing can be obtained by using only one row of sensors on the model surface. The model is rotated with a certain roll angle in one direction while the sail is rotated in the opposite direction with the same amount. By this action, while changing the circumferential location of the row of sensors, the model geometry and the alignment relative to the free-stream for a specific pitch angle and sail location is kept constant. A small gap between the model and the sail has been kept in order the sail to be moved on top of the sensors without any contact. This gap has been sealed properly and without giving any fillet effect for every roll angle before the data were taken.

In order fix the transition location on the model and further guarantee a Reynolds-number insensitive separation, trip posts of 0.76 mm high cylinders with 1.28 mm diameter, 2.5 mm spaced apart, were placed on the model nose part at  $x/L = 0.10$ . Two rows of the same trip posts were put on the lower and the upper surfaces of the sail in the spanwise direction. The rows were located 0.64 cm (measured on the surface) away from the leading edge of the sail.

### II.C. Hot-film Sensors and the Calibration

To measure the skin friction, hot-film sensors designed and documented by Simpson et al.<sup>7</sup> are used. The sensors are made of Balco foil (70% nickel, 30% iron) and the main sensing part is a spiral of 5.1 mm in diameter. These directionally insensitive hot-film sensors have been designed to measure the magnitude of the skin friction as described in Simpson et al.<sup>7</sup> The sensors heat the near-wall fluid by forced convection. Because of the similarity between the gradient transport of momentum and scalars (heat), heat transfer in the fluid gives a measure of the wall shear. The mean film coefficient  $\bar{h}$  is proportional to the cube root of the near wall velocity gradient which is thus proportional to the wall shear  $\tau_w$ . Hot-film sensors are operated with Miller-type non-linearized constant-temperature anemometers.<sup>8</sup> The same sensor-anemometer set-up was used by Wetzel<sup>2</sup> in his prolate spheroid study. He reported a flat frequency response

out to roughly 200 Hz. Because of relatively low frequency response and large sensor size (diameter of 5.1 mm), the sensors are insensitive to high-frequency, small-scale turbulent fluctuations. However, the frequency response is high enough to resolve the time-history of the spatially-averaged skin friction values in unsteady maneuvers.

The hot-film sensors that are used in the actual tests have been calibrated on the constant diameter part of the model at zero angle of attack. By removing the sail during the calibrations, axi-symmetric flow around the model was maintained. Boundary Layer velocity profiles on the constant diameter region of the model were taken in four calibration speeds: 24.4 m/s, 29 m/s, 33.5 m/s and 42.7 m/s. Measurements for each speed were made at two stations. The first station was at the upstream location of the constant diameter region ( $x/L = 0.25$ ) and the second station at the downstream part ( $x/L = 0.59$ ). By using the boundary layer velocity profiles, the boundary layer thickness  $\delta$ , displacement thickness  $\delta^*$ , momentum thickness  $\theta$  and the shape factor  $H$  at each station have been calculated by taking into account the transverse wall curvature effect which was discussed in White.<sup>9</sup> The velocity measurements in the streamwise direction between these two stations also showed that the boundary layer edge velocity  $U_e$  could be taken as constant along the constant diameter region of the model. To determine the  $\theta$  distribution between two measurement stations, the following momentum integral equation has been used:

$$0.03138 \left[ Re_a \ln \left( 1 + 9.337 \frac{\theta}{a} \right) \right]^{-0.2857} = \frac{d\theta}{dx} \quad (2)$$

This equation has been obtained by using the approach in Kays and Crawford<sup>10</sup> and making necessary modifications to include the transverse curvature effects. Equation 2 which represents an initial value problem, has been solved numerically by using *Modified Euler's Method* in order to determine the momentum thickness distribution. As the initial value for the momentum thickness, the  $\theta$  value measured at the second station has been used. After obtaining the  $\theta$  distribution, skin friction coefficient at each sensor location has been obtained by using *Ludwig-Tillmann equation*:

$$\frac{C_f}{2} = 0.123 \times 10^{-0.678H} \left( \frac{U_e \theta}{\nu} \right)^{-0.268} \quad (3)$$

The calibration  $C_f$  values were obtained for  $1010 \leq Re_\theta \leq 4900$ . For the calibration, the hot-film version of King's Law has been used:

$$\frac{E^2}{(T_w - T_\infty)} = A + B(\tau_w)^{1/3} \quad (4)$$

Here,  $E$  is the time-averaged voltage value obtained from a hot-film sensor connected to a constant temperature anemometer,  $T_w$  stands for the sensor temperature and  $T_\infty$  for free-stream temperature of the flow in the tunnel. The purpose of the calibration is to determine the

coefficients  $A$  and  $B$  in equation 4. For finding these coefficients,  $E$  and corresponding  $\tau_w$  values obtained at the calibration speeds have been used to make a linear regression. In equation 4, the change in the free-stream temperature will also cause a change in the calibration coefficients  $A$  and  $B$ . Since the temperature of the stability tunnel is ambient and can not be controlled, the calibration procedure was repeated as the tunnel temperature changed. In order to minimize the uncertainty in the skin friction measurements due to the free-stream temperature change for the barebody case, the calibration coefficients for each sensor have been re-calculated for every roll angle position of the model before taking steady data and performing unsteady maneuvers for that specific roll angle. The free-stream temperature change was at most  $\pm 0.5$  C° between each roll angle position and this was included in the overall uncertainty calculations. For the measurements with the sail, calibration coefficients for each sensor were re-calculated approximately in every 10 roll angle by simply detaching the sail from the body and applying the calibration procedure to the barebody.

#### II.D. Steady Measurements and the DyPPiR Maneuvers

All the skin friction measurements were done with a tunnel speed of  $42.7 \pm 1\%$  m/s. For these experiments, the Reynolds number based on the model length  $Re_L$  was  $5.5 \times 10^6$ . The oil flow visualizations were taken at  $Re_L = 4.5 \times 10^6$ .

Measurement of the skin friction in steady experiments and unsteady maneuvers has been performed for two model configurations: barebody and sail-on-side cases. In the barebody case, both steady and unsteady skin friction data were acquired between  $\phi = 0^\circ$  and  $180^\circ$  in the circumferential direction with  $10^\circ$  increments on the windward side and for every  $2^\circ$  on the leeward side. For the sail-on-side case, measurements were made between  $\phi = 0^\circ$  and  $360^\circ$ . The  $\phi$  increment was again  $2^\circ$  on the leeward side in order to locate the crossflow separation locations with low uncertainty. On the windward side, measurements were made with  $10^\circ$  increments except the region between  $\phi = 270^\circ$  and  $292^\circ$  where  $C_f$  was measured every  $2^\circ$  so as to resolve the surface flow structure in the vicinity of the sail.

Steady hot-film measurements were taken at 14 angles of attack starting from  $0.9^\circ$ . The angle of attack increment was  $2^\circ$  and the last angle covered was  $27.6^\circ$ . These angles are shown by solid square symbols in figure 5. Besides obtaining the steady surface flow structure over the model, the results of the steady data at these angles of attack were also used to construct the quasi-steady data to be used in a first-order lag model which will be described in Section III below.

Unsteady results were obtained for the pitchup maneuvers. The pitchup maneuver performed for the present work is a simple linear ramp from  $1^\circ$  to  $27^\circ$  in 0.33 seconds. Figure 5 shows the DyPPiR pitch angle

and plunge location feedback for the pitchup maneuvers. The DyPPiR pitch angle is also the instantaneous angle attack measured at the model center of rotation. Note that the actual maneuver starts at  $t' = 3.00$ . The maneuvers were performed with a constant pitch rate of  $78^\circ/s$  and the model center of rotation was at  $x_{cg}/L = 0.24$ . For each  $\phi$  orientation of the model, the pitchup maneuver was executed for 10 times. Unsteady skin friction values at each  $x/L$  measurement station has been calculated for each repetition and the final value was obtained by ensemble averaging the skin friction values. Further details about the unsteady data reduction procedure may be found in Hosder.<sup>5</sup>

#### II.E. Uncertainties in Measured Quantities

The skin friction magnitudes measured on the leeward side of the model have an uncertainty of  $\pm 5\%$  for random uncertainties at 20:1 odds. On the windward side, uncertainty in the skin friction magnitudes is  $\pm 10\%$ . The uncertainty in the determination of the separation locations is  $\pm 2^\circ$ .

### III. Results and Discussion

#### III.A. Steady Results

For the range of conditions mentioned above, steady results over the barebody show typical characteristics of the crossflow separation. Figure 6 shows the oil flow visualization of the near-wall fluid over the constant diameter region of the model in the barebody case and qualitatively describes the crossflow separation topology. Skin-friction lines converge along the separation lines and from this figure two separation lines can be identified on the leeward side of the model. The one closer to the windward side is defined as the primary separation and the other as the secondary separation line.

Figure 7 gives the skin-friction  $C_f$  distribution vs. circumferential location on the model surface  $\phi$  at  $\alpha = 15.3^\circ$  for different  $x/L$  stations. Barebody results are represented by the filled symbols. At this pitch angle,  $x/L = 0.266$  is the first station at which a minimum in the  $C_f$  distribution can be detected. This minimum indicates the primary separation location at  $\phi = 146^\circ$ . Starting from this station, the primary separation can be clearly seen as the most windward of the  $C_f$  distribution at all the other  $x/L$  stations downstream. As  $x/L$  increases, the primary separation location moves towards the windward side. It is also interesting to see the nearly flat profile at the vicinity of the minimum point for the last station  $x/L = 0.863$  located on the stern region. This profile indicates separated low speed fluid in this complex flow region between  $\phi \simeq 100^\circ$  and  $130^\circ$  which makes the identification of the true minimum difficult. The secondary separation location can be obtained by finding the second minimum in each  $C_f$  vs  $\phi$  distribution after a certain pitch angle. At  $\alpha = 15.3^\circ$ , the secondary separation can clearly be observed starting from

$x/L = 0.638$ . The secondary separation location moves in the leeward direction as  $x/L$  increases.

Figure 9 shows the  $C_f$  vs.  $\phi$  distribution for all the pitch angles covered in the steady measurements at  $x/L = 0.501$ , both for barebody and sail-on-side case. In the barebody case,  $\alpha = 7.2^\circ$  is the first pitch angle at which a primary separation has been observed at  $\phi = 146^\circ$ . As  $\alpha$  increases, the primary separation location moves windward and reaches to  $\phi = 120^\circ$  at  $\alpha = 27.6^\circ$ . The secondary separation can be identified starting from  $\alpha = 15.3^\circ$  and moves leeward with increasing pitch angle. The results given above indicate that at a specific  $x/L$  station, the primary separation location moves windward while the secondary separation location in the leeward direction as  $\alpha$  is increased. At a certain pitch angle, the primary separation location will move windward and the secondary separation location leeward as we go downstream in  $x/L$ .

In figures 7 and 9, open symbols stand for the  $C_f$  vs.  $\phi$  distributions of the sail-on-side case. It is more appropriate to evaluate the results of the sail-on-side case in two separate regions; the region with no sail (between  $\phi = 0^\circ$  and  $180^\circ$ ) and the region with the sail (between  $\phi = 180^\circ$  and  $360^\circ$ ). In the first region, the origin and the variation of the primary and the secondary separation lines as a function of  $x/L$  and  $\alpha$  show the same characteristics as defined for the barebody case. This implies that the main flow feature on the non-sail region is the cross flow separation. Although the general trend is the same, in figure 7, for the stations  $x/L \geq 0.501$  at  $\alpha = 15.3^\circ$ , the locations of the primary and the secondary separations are slightly different from the barebody separation locations. They are more leeward compared to the barebody locations. The same difference can also be observed in figure 9 for  $\alpha \geq 15.3^\circ$  at  $x/L = 0.501$ . Figure 8 shows the variation of the primary separation location with  $\alpha$  for three different  $x/L$  stations. As can be seen from this figure, the primary separation locations of the barebody case and the non-sail region of the sail-on-side case are approximately the same within uncertainties up to  $\alpha = 15.3^\circ$ . Beyond this angle, the separation locations of the sail-on-side case start to deviate from the barebody results having an offset in the leeward direction. This difference is obvious for  $\alpha = 21.4^\circ, 23.4^\circ$  and  $25.5^\circ$ .

The flow structure on the sail side of the model is much different than the one observed for the non-sail side. The flowfield in this region is strongly affected by the presence of the sail. In figure 7, in the sail region, a minimum can be located at four stations:  $x/L = 0.306, 0.345, 0.434$  and  $0.501$ . Corresponding  $\phi$  locations are  $224^\circ, 220^\circ, 212^\circ$  and  $210^\circ$ . This may indicate a separation at these stations. However, for the rest of the stations downstream, this minimum vanishes. A second minimum in  $C_f$  can be seen at  $x/L = 0.345$  and the rest of the stations downstream. This minimum has an approximately constant  $\phi$  location of  $256 \pm 2^\circ$  between  $x/L = 0.501$  and the last station  $x/L = 0.863$ . The same trend can also be observed in figure 9. A minimum in  $C_f$  for  $\alpha = 9.3^\circ, 11.3^\circ, 13.2^\circ$  and  $15.3^\circ$  at  $\phi = 216^\circ, 216^\circ,$

$208^\circ$  and  $208^\circ$  respectively can clearly be located. The second minimum starts from  $\alpha = 5.1^\circ$  and has a constant circumferential location of  $256^\circ \pm 2^\circ$  between  $\alpha = 13.2^\circ$  and  $27.6^\circ$ . The results on the sail side indicate that the flowfield does differ from the crossflow separation structure observed for the barebody and non-sail region of the sail-on-side case. Therefore the categorization of the separation locations as the primary or the secondary is not clear and may not reflect the real flow structure of this region.

The flow in the vicinity of the sail-body junction is dominated by the horseshoe type separation. This can be clearly seen from figure 10 which shows the oil-flow pattern in the leeward side of the sail region at  $\alpha = 15^\circ$ . The separation line emanating from a three-dimensional stagnation point upstream of the sail extends from both leeward and windward side of the sail and travels downstream. The separation line on the leeward side of the sail can be seen along the converging skin friction lines in figure 10. Although the flow topology near the onset of the horseshoe separation is different from that of the crossflow separation,<sup>11</sup> both show similar characteristics of separated flows downstream: there is a strong convergence of the limiting streamlines on the surface and there are concentrated regions of vorticity in the flow. This may raise the ambiguity about the identification of the separation pattern downstream of the sail. Figure 11, shows the  $C_f$  contours around the sail region at  $\alpha = 15.3^\circ$ . Note that the blank areas are the regions where no data were acquired. The vertical blank between  $x/L \simeq 0.22$  and  $x/L \simeq 0.26$  designates the ring area where the sail is mounted. In this plot, a low velocity region can be noticed at around  $x/L = 0.27$  and  $\phi = 245^\circ$  which also matches with the oil flow visualization results at that location.  $C_f$  on the hull takes relatively large values at regions closer to the sail.

### III.B. Unsteady Results

In this paper, the unsteady results will be presented for the barebody case. One of the methods to investigate the difference between the steady and the unsteady flow over the model is to compare the steady  $C_f$  vs.  $\phi$  distribution obtained at a certain pitch angle  $\alpha$  with the unsteady one acquired at the corresponding instantaneous pitch angle  $\alpha(t')$  for a specific  $x/L$  location. Figures 12 and 13 show this comparison for  $x/L = 0.501$  at  $\alpha = 21.4^\circ$  and  $25.4^\circ$  respectively. At both angles of attack, the unsteady separation location differs from the steady one. In figure 12, the primary separation location for the steady data is  $\phi = 122^\circ$ , while the unsteady primary separation occurs at  $\phi = 138^\circ$ . The steady data have a secondary separation at  $\phi = 148^\circ$  while no secondary separation is observed for the unsteady case at this angle of attack. The difference between the  $C_f$  magnitudes should also be noted. Especially in the leeward region between  $150^\circ$  and  $180^\circ$  this difference is significant, with steady values being higher than the unsteady ones. In figure 13, for  $\alpha = 25.5^\circ$ , again the dif-

ference in the location of the primary separation can be seen. A premature development of secondary separation at  $\phi = 142^\circ$  should also be noted for the unsteady case.

These results show that in unsteady flows the separation topology is different from the one in an equivalent steady configuration. This difference originates from the fact that the unsteady separation location lags the steady separation. This can be clearly seen from the figures 15, 16 and 17 where the quasi-steady and the unsteady primary separation locations are plotted against the non-dimensional time  $t'$  for different  $x/L$  stations. In all three figures, the horizontal distance between the unsteady and the steady separation location is an indication of the presence of a timelag. Since the maneuvers were performed with a constant pitch rate, the instantaneous pitch angle is a linear function of  $t'$ . By considering this fact in examining figures 15, 16 and 17, it can also be thought that at an instantaneous pitch angle, for a specific  $x/L$  location, the unsteady separation starts more leeward compared with the steady case. This explains the cause of difference between the steady and the unsteady separation locations shown in figures 12 and 13.

To understand, why a lag exists; as described by Wetzel and Simpson,<sup>3</sup> one should examine the path of a fluid particle during the maneuver. During the pitchup maneuver, a fluid particle originally starts its trajectory on the windward side of the model at a lower angle of attack. Therefore, the particle experiences a less severe adverse pressure gradient along its path, and can travel farther around the leeside before separating when compared with a similar particle in a steady flowfield.

The main interest is to be able to model or approximate the time lags associated with the unsteady flowfields. Algebraic time lag modelling was a commonly used approach in the previous studies. Most of the algebraic time lag models are based on finding an effective angle of attack  $\alpha_{eff}$  by using the descriptions of the flow kinematics. If a model rotates about some point  $x_{cg}$  at a constant pitch rate  $\dot{\alpha}$ , a relative velocity normal to the model axis  $\dot{\alpha}(x - x_{cg})$  will exist at other  $x/L$  locations in addition to the velocity of the wind relative to the point of rotation. By using this fact, Montividas et al.<sup>12</sup> approximated an effective angle of attack as:

$$\alpha_{eff} = \alpha - \Delta\alpha_{eff} \quad (5)$$

where

$$\Delta\alpha_{eff} = \dot{\alpha} \frac{x_{cg} - x}{U_\infty} \quad (6)$$

However, this approximation did not describe the unsteady effects in their flowfield associated with the onset of asymmetric vortex shedding at high angles of attack on ogive cylinders. Ericsson<sup>13</sup> also studied the same problem and extended the effective angle of attack idea by including convective lag effects in the flowfield. He used the fact that a vortex at a downstream station of the apex of the model (ogive cylinder) will react to the changed flow conditions at the apex at a time  $\Delta t$  later. He also approximated that the disturbances originating at the apex of the model would propagate down-

stream with the free-stream velocity  $U_\infty$  which would give  $\Delta t = x/U_\infty$ . By using this result in equation 6, Ericsson<sup>13</sup> obtained:

$$\Delta\alpha_{eff} = \dot{\alpha} \frac{x_{cg} + x}{U_\infty} \quad (7)$$

Equation 7 did approximate the lags in asymmetric vortex shedding on the pitching ogive cylinder successfully.

In this study,  $\Delta\alpha_{eff}$  has been calculated both from the experimental results and equation 7 for four different  $x/L$  locations. Since the pitch rate has a constant value of  $78^\circ/s$ , the lag equation 7 gave constant  $\Delta\alpha_{eff}$  values for each  $x/L$  locations. For calculating  $\Delta\alpha_{eff}$  from the experimental results, certain number of unsteady separation locations  $\phi_{sep}$  and corresponding instantaneous pitch angles  $\alpha(t')$  have been selected from the data. Then the same  $\phi_{sep}$  values for the steady data and the corresponding steady pitch angles have been picked. For a specific  $\phi_{sep}$ , the difference between the instantaneous pitch angle and the steady pitch angle has been calculated as the effective angle of attack increment. The  $\Delta\alpha_{eff}$  results obtained from equation 7 and the experimental data have been compared in figure 14. As can be seen from this figure, there is a significant difference between experimental  $\Delta\alpha_{eff}$  and the one calculated from equation 7. Especially for the stations  $x/L \geq 0.501$ , the magnitudes of the experimental  $\Delta\alpha_{eff}$  are twice as much higher than that of obtained by using the model equation 7. Also, although the the pitch rate is constant, experimental  $\Delta\alpha_{eff}$  does change with the instantaneous pitch angle thus with the time. This comparison shows the difference between the lags in the unsteady crossflow separation over the model used in the present experiment and the flowfield associated with the asymmetric vortex shedding on the ogive cylinder.

Goman and Khrabov<sup>14</sup> have developed a first order time lag model in order to approximate the time history of a dominant flow feature such as separation location in general unsteady flows. They applied this model to pitching two-dimensional airfoils, delta wings and the unsteady aerodynamics of a complex fighter aircraft configuration as well. They used the separation location as an internal state variable, and defined the forces and moments as functions of this state variable. For a given maneuver, by obtaining the time history of this state variable, they were able to calculate the unsteady force and moments.

Wetzel and Simpson<sup>3</sup> implemented an extended version of this model for approximating the time varying nature of the unsteady separation locations over the maneuvering prolate spheroid. The approximation successfully fit the experimental unsteady separation locations and non-dimensional time lag values for different  $x/L$  stations of the prolate spheroid were obtained. The same extended version of the first-order differential lag model has been used in this study in order to approximate the unsteady primary separation locations over the model without sail undergoing pitchup maneuvers:

$$\tau' \left( \frac{x}{L} \right) \frac{d\phi_{uns}}{dt'} + \phi_{uns} \left( \frac{x}{L}, t' \right) = \phi_0 \left( \frac{x}{L}, \alpha(t') \right) \quad (8)$$

In equation 8,  $\phi_{uns}$  represents the approximation to the unsteady separation location and  $\tau'$  stands for the first-order non-dimensional time lag.  $\phi_0$  is the quasi-steady separation location distribution which can be obtained from the steady separation data at each  $\alpha = \alpha(t')$ . Note that both the quasi-steady separation location  $\phi_0$  and the approximation to the unsteady separation location  $\phi_{uns}$  do also vary in  $x/L$ . This is the difference between the extended version and the original time lag model of Goman & Khrabov.<sup>14</sup> In the original version, a single point of separation was considered. However, for the present study and the prolate spheroid case, since the crossflow separation occurs along a line rather than a point,  $\phi_{uns}$  and  $\phi_0$  were also functions of  $x/L$ . It should also be noted that the time lag  $\tau'$  in equation 8 is taken as an unknown and is identified by fitting the model equation with the experimental data.

Equation 8 mainly correlates the unsteady separation locations to the quasi-steady data by the time lag  $\tau'$ . In the solution procedure, the quasi-steady separation distribution  $\phi_0$  was obtained by fitting a cubic spline to the steady data. The independent variable was  $t'$  in the fitting procedure. As the initial value for  $\phi_{uns}$ , the first steady separation location in the steady data was used. For each  $x/L$  station, the model equation was solved with different values of the  $\tau'$  in an iterative manner. The root mean square error between the approximated and experimental unsteady data was calculated at each iteration and the  $\tau'$  that gives the smallest error has been chosen for that specific  $x/L$  location. The details of the solution procedure can be found in Hosder.<sup>5</sup> Figures 15, 16 and 17 show the results of the timelag model approximation to the unsteady data at  $x/L = 0.306, 0.570$  and  $0.774$ , respectively. In these figures, the first-order lag model approximation fits the measured unsteady separation locations reasonably well.

$\tau'$  values obtained from the model equation fits for different  $x/L$  locations are shown in figure 18. Note that all the stations were not used in calculating the timelags. At the stations  $x/L \leq 0.266$ , no unsteady separation location at any instant of time was observed. At the last station  $x/L = 0.863$ , the determination of the unsteady separation location was not accurate enough because of the flat nature of the  $C_f$  profile near the minimum, as discussed in the steady results section. In figure 18, near the model rotation point  $x_{cg}/L = 0.24$ , time lag value is close to zero indicating that the quasi-steady data follows the unsteady data closely. Then an increase until  $x/L = 0.43$  can be seen. Since there are not enough points in this region, the nature of this increase (linear or non-linear) can not be determined accurately. After this point, the time lag stays approximately constant between  $x/L = 0.43$  and  $x/L = 0.774$ , taking an average value of 1.40. At  $x/L = 0.819$ , this value drops to 1.24.

The trend that  $\tau'$  distribution follows in this study is different from the one obtained for the prolate spheroid by Wetzal and Simpson.<sup>3</sup> In that case,  $\tau'$  changed approximately in a linear manner increasing in downstream direction over the prolate spheroid model. However, for

their pitchup maneuvers, the model center of rotation point was at  $x/L = 0.5$ , whereas in this study the rotation point is at  $x/L = 0.24$ . Also the Suboff model has a different geometry than the prolate spheroid, having a large proportion of a constant diameter region. Therefore, one may expect an influence of the rotation point and the model geometry on the time lags. However further study has to be done in order investigate the true complex nature of the time lags associated with the unsteady flowfield over this undersea vehicle geometry.

## IV. Conclusions

Steady and unsteady skin friction magnitudes have been measured over the Suboff model by using hot-film sensors. The minima of the skin friction vs.  $\phi$  distribution at each  $x/L$  measurement station have been used to locate the separation locations. The steady results obtained for the barebody case show that the flow on the leeward side of the model can be characterized by the crossflow separation. For the sail-on-side case, the steady flow over the non-sail region of the model also show the basic characteristics of the crossflow separation, and the  $C_f$  vs.  $\phi$  distributions follow the barebody results closely. The flow structure on the sail side is strongly affected by the presence of the sail. The oil flow pictures show the horseshoe type of flow separation around the sail. The separation location variation as a function of  $\alpha$  and  $x/L$  is different from the one obtained for the barebody case. Therefore, the flowfield on the sail side may not be characterized by the crossflow separation.

The unsteady data over the barebody show that the unsteady separation topology is different from the one observed in the steady case. At the same angle of attack, no secondary separation location was observed for the unsteady data whereas the steady data have both primary and secondary separations. Unsteady data also showed significant time lags between the unsteady and steady flow separation locations. Algebraic time lag model results did not match with the experimental results. This indicates the complex nature of the unsteady flow separation over the Suboff model. The first-order time lag model of Goman and Khrabov fit the unsteady data reasonably well. Time lags obtained from this model have a unique variation along  $x/L$  that does not match with the one obtained for the prolate spheroid geometry.<sup>3</sup> The model center of rotation and the geometry are different between two cases. This may imply the influence of these two parameters on the time lags.

## Acknowledgments

The present work was supported by Office of Naval Research (ONR) grants N0014-96-1-0969 and N0014-99-1-0428, Dr. L. P. Purtell, Program Manager. The oil flow visualizations were performed by Dr. T. G. Wetzal. The data will be available on the AOE Virginia Tech website.

## References

- [1] Simpson, R. L. Unsteady Aero-Hydrodynamics for Maneuvering Aircraft, Submarines and Automobiles. Report VPI-AOE 253, Department of Aerospace and Ocean Engineering, Virginia Tech, November 1997.
- [2] Wetzel, T. G. *Unsteady Flow over a 6:1 Prolate Spheroid*. PhD thesis, Department of Aerospace and Ocean Engineering, Virginia Tech, Blacksburg, VA 24061, April 1996.
- [3] Wetzel, T. G. and Simpson, R. L. Unsteady Crossflow Separation Location Measurements on a Maneuvering 6:1 Prolate Spheroid. *AIAA Journal*, 36(11):2063–2071, November 1998.
- [4] Etkin, B. *Dynamics of Atmospheric Flight*. Wiley, New York, 1972.
- [5] Hosder, S. Unsteady Surface Flow Measurements on the Darpa2 Suboff Body. M.S. Thesis, Department of Aerospace and Ocean Engineering, Virginia Tech, 2001 (expected).
- [6] Wetzel, T. G., Simpson, R. L., and Chesnakas, C. J. Measurement of Three-Dimensional Crossflow Separation. *AIAA Journal*, 36(4):557–564, April 1998.
- [7] Simpson, R. L., Walker, D. A., and Shinpaugh, K. A. Description of a 1000 Sensor Constant Current Anemometer System for Locating Three Dimensional Turbulent Boundary Layer Separations. Report VPI-AOE 185, Department of Aerospace and Ocean Engineering, Virginia Tech, December 1991.
- [8] Miller, J. A. A Simple Linearized Hot-Wire Anemometer. *Journal of Fluids Engineering*, 98(3):550–557, 1976.
- [9] White, F. M. An Analysis of Axisymmetric Turbulent Flow Past a Long Cylinder. *ASME Journal of Basic Engineering*, 94:200–206, March 1972.
- [10] Kays, W. M. and Crawford, M. E. *Convective Heat and Mass Transfer*. McGraw-Hill, New York, 1980.
- [11] Yates, L. A. and Chapman, G. T. Streamlines, Vorticity Lines and Vortices Around Three Dimensional Bodies. *AIAA Journal*, 30(7):1819–1826, July 1992.
- [12] Montividas, R. E., Reisenhel, P., and Nagib, H. N. The scaling and Control of Vortex Geometry Behind Pitching Cylinders. *AIAA Paper 89-1003*, 1989.
- [13] Ericsson, L. E. Unsteady Flows. In *Tactical Missile Aerodynamics: General Topics*, pages 490–493. edited by M. J. Hemsch, Progress in Astronautics and Aeronautics, AIAA, Washington D.C., 1992.
- [14] Goman, M. and Khrabov, A. State-Space Representation of Aerodynamic Characteristics of an Aircraft at High Angles of Attack. *Journal of Aircraft*, 31(5):1109–1115, 1994.

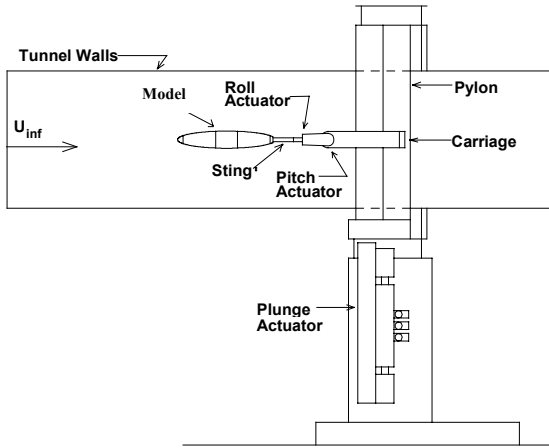


Figure 1. Dynamic Plunge-Pitch-Roll (DyPPiR) Model Mount installed in the wind tunnel. (taken from Wetzel<sup>11</sup>)

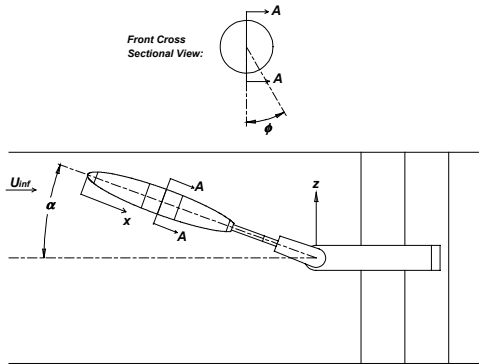


Figure 2. Coordinate Nomenclature.  $x$  is measured from the nose;  $\phi$  is the circumferential location measured from the windward line of symmetry;  $z$  is the plunge ordinate; and  $\alpha$  is the pitch angle and equivalently the model center angle of attack. (taken from Wetzel<sup>11</sup>)

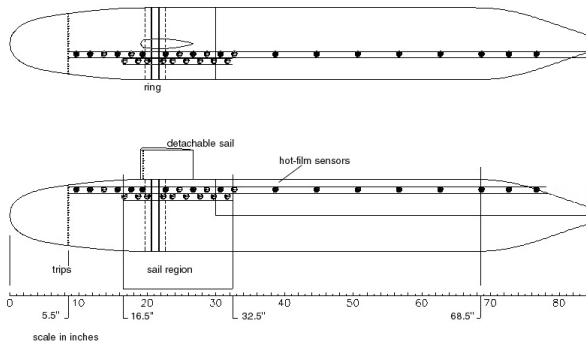


Figure 3. Top and side view of the model and hot-film sensor locations.

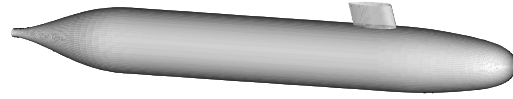


Figure 4. 3-D view of the suboff model with the sail

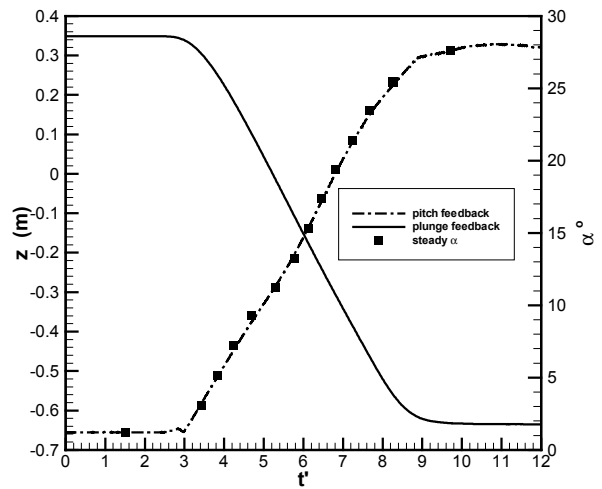


Figure 5. Dyppir plunge and pitch feedback for the pitchup maneuvers. Filled symbols show the  $\alpha$  locations for the steady measurements.

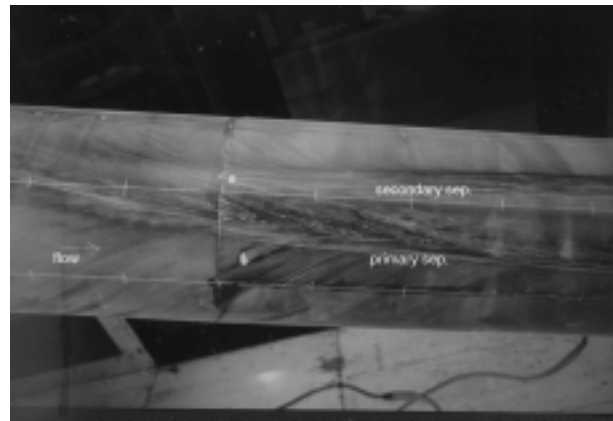


Figure 6. Oil flow visualization showing the crossflow separation topology on the constant diameter region of the model without sail at  $\alpha=20^\circ$ ,  $Re=4.5 \times 10^6$ . Flow is from left to right.

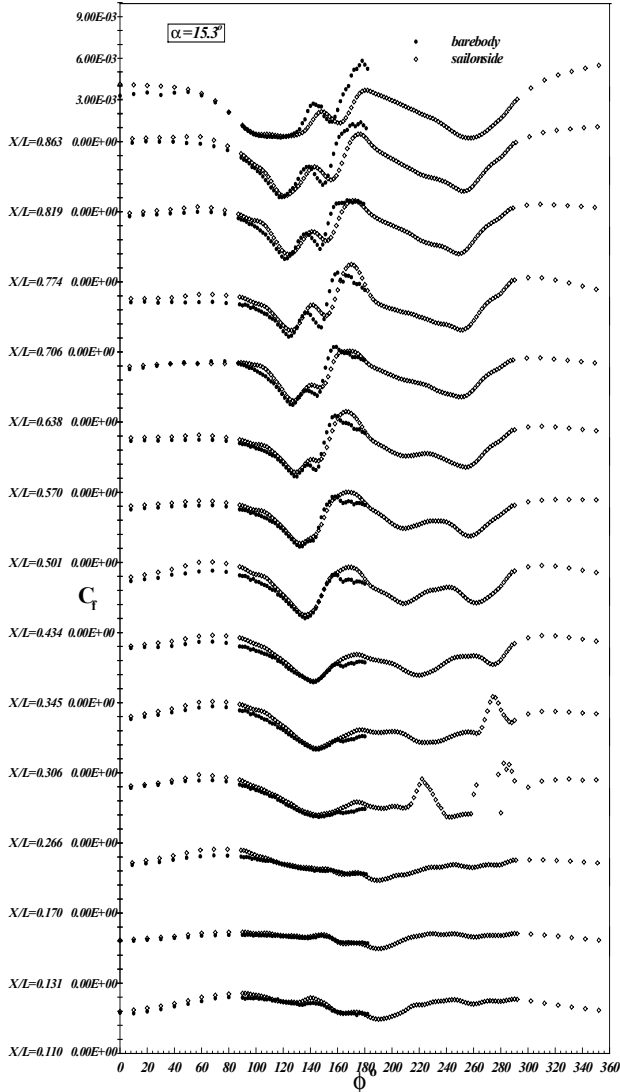


Figure 7.  $C_f$  vs.  $\phi$  for all  $x/L$  locations at  $\alpha=15.3^\circ$  for steady barebody and sailside cases. Sail side on the right of the figure.

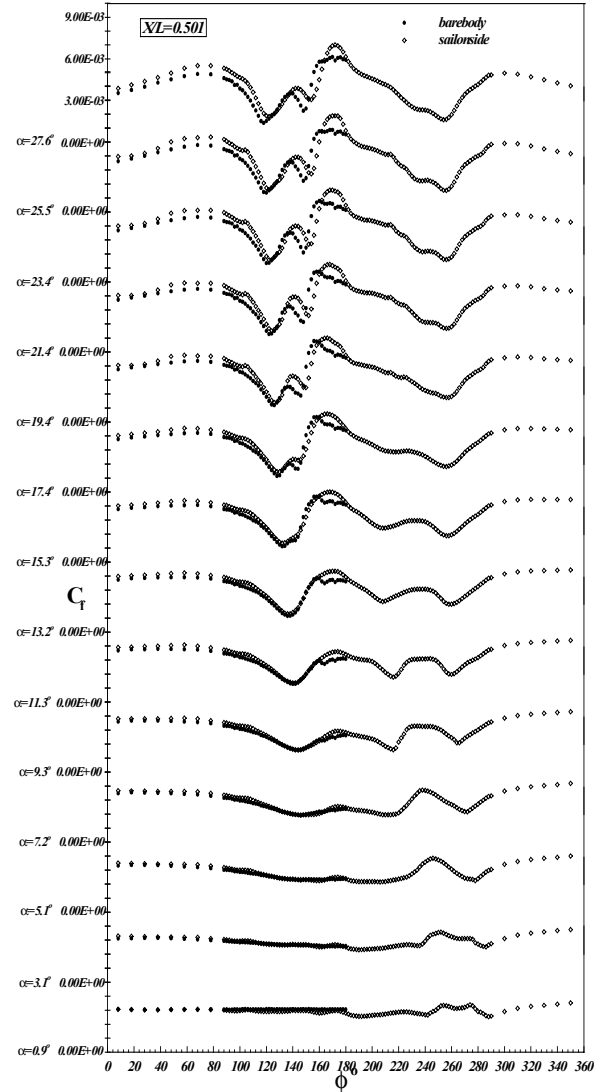


Figure 9.  $C_f$  vs.  $\phi$  for all  $\alpha$  at  $x/L=0.501$  for steady barebody and sailside cases. Sail side on the right of the figure.

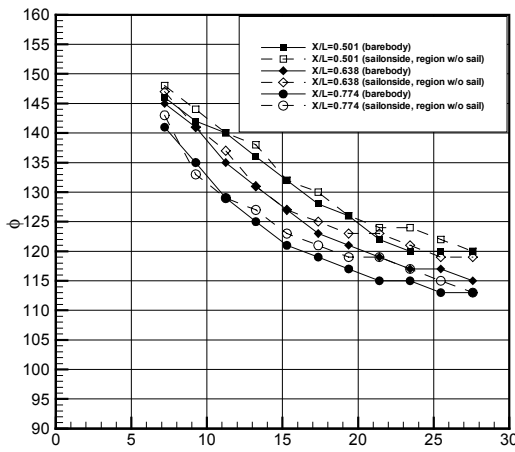


Figure 8. Steady primary separation locations vs.  $\alpha$  for barebody and sailside (region without sail) case at  $x/L=0.501, 0.638$  and  $0.774$ .

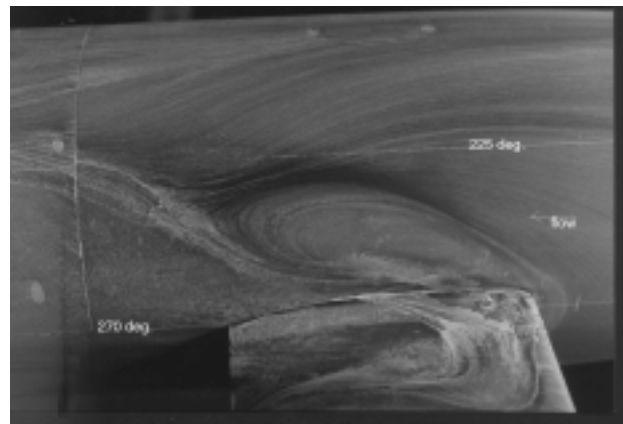


Figure 10. Oil flow pattern showing the separation in the vicinity of the sail at  $\alpha=15^\circ$ ,  $Re=4.5 \times 10^6$ . Flow is from right to left.

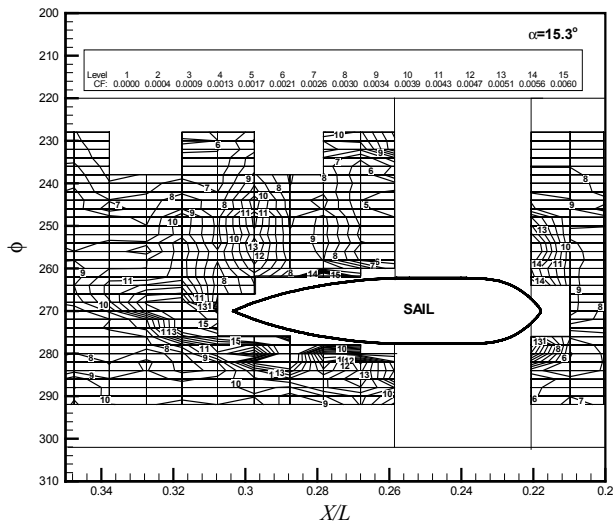


Figure 11. Steady  $C_f$  contours in the vicinity of the sail at  $\alpha=15.3$ .

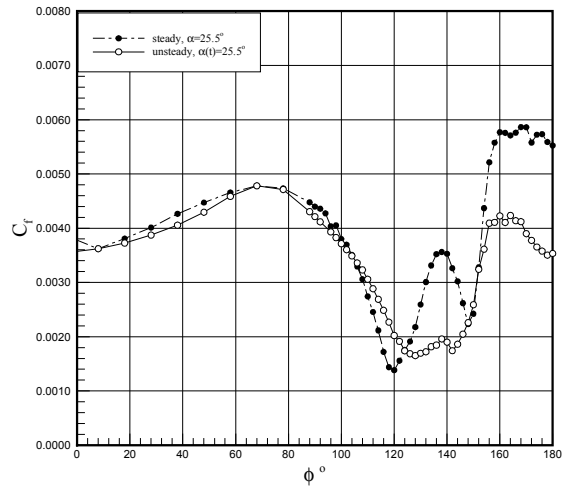


Figure 13. Comparison of  $C_f$  vs.  $\phi$  distribution for steady and unsteady data for barebody case.  $\alpha=25.5^\circ$ ,  $x/L=0.501$ .

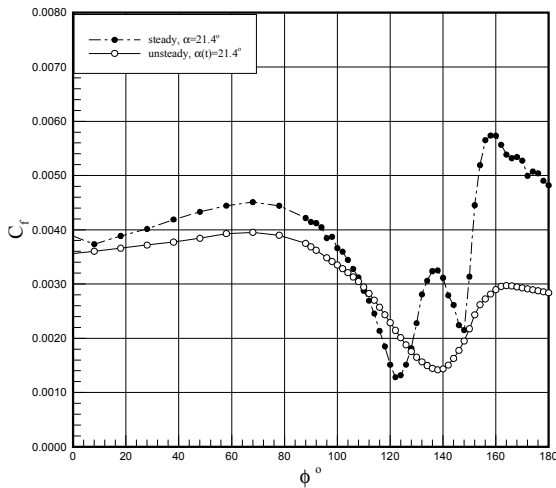


Figure 12. Comparison of  $C_f$  vs.  $\phi$  distribution for steady and unsteady data for barebody case.  $\alpha=21.4^\circ$ ,  $x/L=0.501$ .

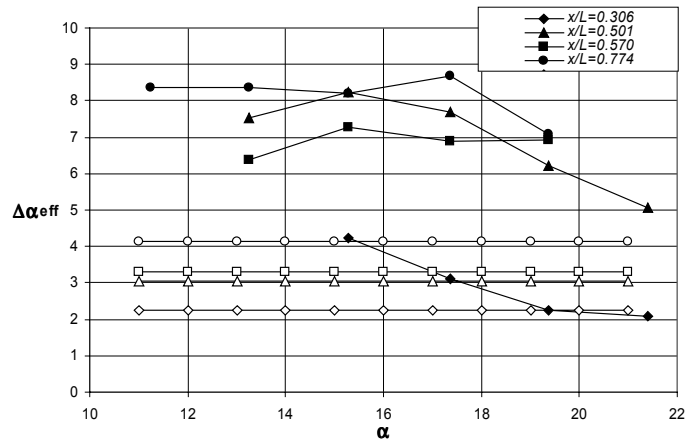


Figure 14. Incremental effective angle of attack  $\Delta\alpha_{eff}$  for the pitchup maneuver at four  $x/L$  stations as a function of instantaneous angle of attack (Dyppir pitch angle)  $\alpha$ . Open symbols show the effective angle of attack given by the equation 7. (Both angles are in degrees.)

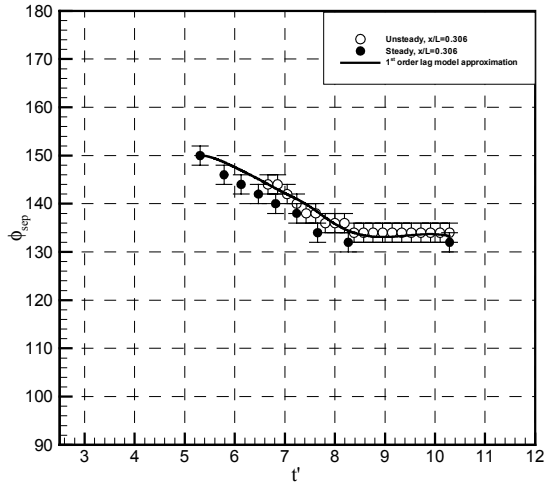


Figure 15. First order differential lag approximation to the unsteady separation data at  $x/L=0.306$ . Solid symbols show quasi-steady data points, open symbols represent unsteady separation locations, lines show the first order lag approximation computed by equation 8.

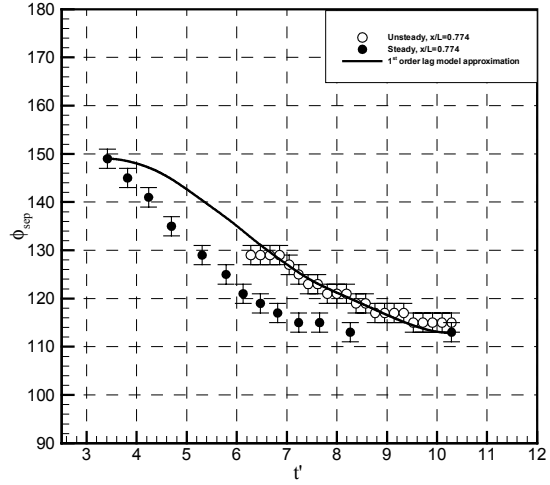


Figure 17. First order differential lag approximation to the unsteady separation data at  $x/L=0.774$ . Solid symbols show quasi-steady data points, open symbols represent unsteady separation locations, lines show the first order lag approximation computed by equation 8.

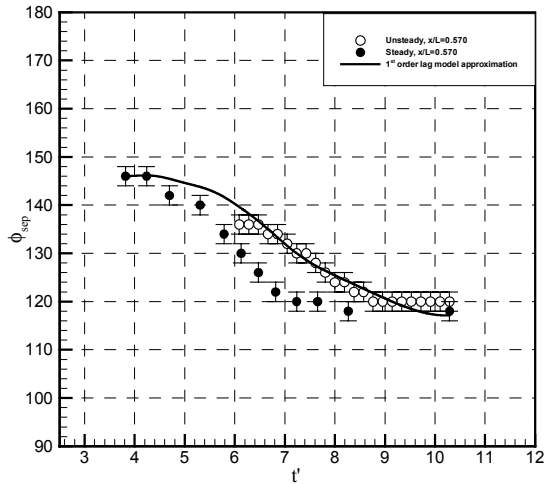


Figure 16. First order differential lag approximation to the unsteady separation data at  $x/L=0.570$ . Solid symbols show quasi-steady data points, open symbols represent unsteady separation locations, lines show the first order lag approximation computed by equation 8.

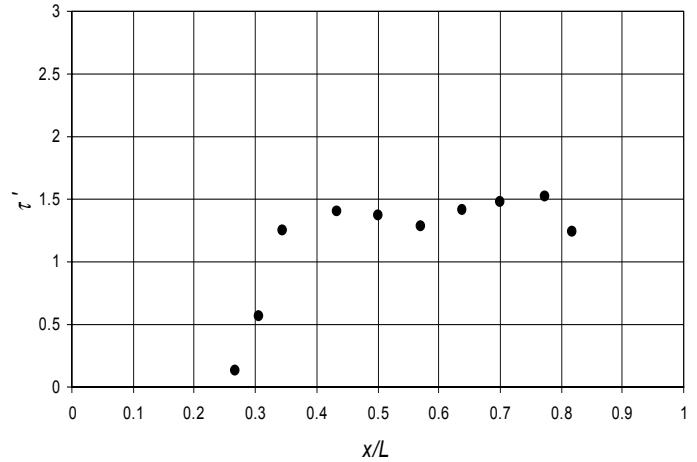


Figure 18. Computed time lags as a function of  $x/L$ .